J. Fluid Mech. (2008), *vol.* 614, *pp.* 355–380. © 2008 Cambridge University Press
doi:10.1017/S0022112008003297 Printed in the United Kingdom

Optimal flexibility of a flapping appendage in an inviscid fluid

SILAS ALBEN
School of Mathematics, Georgia Institute of Technology, Atlanta, GA 30332-0160, USA
alben@math.gatech.edu

(Received 11 January 2008 and in revised form 2 July 2008)

We present a new formulation of the motion of a flexible body with a vortex-sheet wake and use it to study propulsive forces generated by a flexible body pitched periodically at the leading edge in the small-amplitude regime. We find that the thrust power generated by the body has a series of resonant peaks with respect to rigidity, the highest of which corresponds to a body flexed upwards at the trailing edge in an approximately one-quarter-wavelength mode of deflection. The optimal efficiency approaches 1 as rigidity becomes small and decreases to 30–50 % (depending on pitch frequency) as rigidity becomes large. The optimal rigidity for thrust power increases from approximately 60 for large pitching frequency to ∞ for pitching frequency 0.27. Subsequent peaks in response have power-law scalings with respect to rigidity and correspond to higher-wavenumber modes of the body. We derive the power-law scalings by analysing the fin as a damped resonant system. In the limit of small driving frequency, solutions are self-similar at the leading edge. In the limit of large driving frequency, we find that the distribution of resonant rigidities $\sim k^{-5}$, corresponding to fin shapes with wavenumber k. The input power and output power are proportional to rigidity (for small-to-moderate rigidity) and to pitching frequency (for moderate-to-large frequency). We compare these results with the range of rigidity and flapping frequency for the hawkmoth forewing and the bluegill sunfish pectoral fin.

1. Introduction

In many problems of fish swimming and bird and insect flight, propulsive force is obtained by periodic motion of a slender body or appendage (Lighthill 1969; Childress 1981). The body moves in a fluid which is approximately incompressible and which has small dimensionless viscosity (large Reynolds number). Such motions generate sharp concentrations of vorticity which separate from the body and roll up in the fluid, forming a trailing wake of coherent vortices behind the body. The vortices carry fluid momentum, the temporal rate-of-change of which coincides with a forward thrust on the body.

The thrust force and strength of generated vorticity can be calculated in terms of the motion of the body. Many previous studies have calculated the thrust generated by prescribed motions of a rigid or deformable body in a high-Reynolds-number incompressible fluid (Lighthill 1960; Wu 1961; Sparenberg 2002). If the body is flexible, it is deformed by the fluid forces on it, and its motion is not prescribed but is instead determined together with that of the ambient fluid as a coupled dynamical system. These deformations are important in the locomotion of many swimming and flying organisms.

In these coupled flow–body systems, the body motion may be 'active' (set by (1) embedded controlled muscles together with (2) internal elastic forces and (3) forces from the external environment) or 'passive' (determined by (2) and (3) alone). Advantages of passive motions are: (i) simplicity – they do not require complex control strategies for the muscles and (ii) efficiency – they do not require the additional mechanical work for muscular control. Many recent studies of locomotion approach the dynamics and control of locomotory systems from the starting point of passive systems and ask: what dynamics arise naturally from fluid–body interactions with limited or no control? (Vandenberghe *et al.* 2004; Alben & Shelley 2005; Childress, Vandenberghe & Zhang 2006; Fish & Lauder 2006; Bergou, Xu & Wang 2007).

The purpose of this study is to investigate the effect of flexibility on propulsion by a flapping appendage. We focus on a simple body (such as a tail fin or bird or insect wing) driven periodically by a pitching motion at the leading edge. We study the thrust force and efficiency as a function of two dimensionless parameters: the reduced driving frequency at the leading edge and the flexibility of the body.

This study is inspired by a large class of swimming modes where the tail is the dominant source of propulsion. In order of both increasing concentration at the tail, and increasing stiffness of the tail, these motions are: the Subcarangiform, Carangiform, Thunniform and Ostraciiform modes (Lighthill 1969). Such modes involve a relatively straight portion of the body, followed by a more flexible trailing portion of the body and tail fin which oscillates or undulates periodically. Body motions are driven by the contraction of muscles on either side of the backbone. Tail motions are driven by separate muscles in the body which exert a force through tendons onto the leading edges of the tail. These tendons attach onto a scaffold of flexible fin rays which support the tail (Videler 1993).

For slender fish, the flow passing backwards from the straight portion of the body will be nearly as uni-directional as that far upstream. Hence, for simplicity we omit the straight upstream portion of the body and consider a 'disembodied' flexible tail whose leading edge encounters the upstream fluid directly. The method given here can also be used to consider the effect of a straight body segment of varying length placed in front of the tail.

Bainbridge (1963) made diagrams of the kinematics of the tail fin of a swimming dace, and measured the curvature patterns in time. He conjectured a function for the curvature based on steady airfoil theory – that it leads to a forward thrust which is more steady in time than for a rigid plate with the same motion at the leading edge. Curvature also enhances lift forces on airfoils (Thwaites 1987). However, an unsteady model is more appropriate because the flapping frequency non-dimensionalized by U/L (swimming speed U, length L) is not small.

Prempraneerach, Hover & Triantafyllou (2003) studied experimentally the efficiency and forward thrust generated by rubber airfoils driven in a steady stream. For five flexible foils of varying rigidity, they studied a few sets of kinematic parameters which were previously found to give good performance for rigid foils (Triantafyllou *et al.* 1991, 2000). Propulsive efficiency for the flexible foils increased by up to 36 % over the rigid foils, and the maximum thrust coefficient also increased.

Combes & Daniel (2003*a*) measured the bending rigidity of hawkmoth and dragonfly insect wings as a function of distance along the chord and span of the wing. The spatial distribution of bending rigidity was strongly non-uniform, decreasing by more than a factor of 10 from the leading to the trailing edge along the chord, with a similar decrease moving outward along the span. The distribution of rigidity was well-fitted by an exponential. The spanwise stiffness was much greater than chordwise stiffness, so that the primary bending mode is along the chord. Combes & Daniel (2003*b*) used these material parameters as inputs to a finite element model with typical kinematics imposed at the wing root and found significant bending of the model wing.

In the realm of fish swimming, Lauder *et al.* (2006) and Alben, Madden & Lauder (2007) measured the rigidity of fin rays taken from the pectoral fin of Bluegill sunfish. These rays are the primary structural support of the fin. Here too, a strong decay of rigidity was found, moving outward along the ray from its juncture with the fish body to the distal tip. Unlike insect wings, the fin ray has a bilaminate structure which allows some control of its rigidity. We shall consider this structure further in subsequent work. Fish *et al.* (2006) studied experimentally a different passive mechanism for shape change in cetacean tails, which can produce camber with desirable propulsive characteristics. Other studies have considered the stiffness of the fish skin (Long *et al.* 1996), and the fish backbone (Wainwright 2000). The special architecture of the backbone is conjectured to allow efficient passive swimming motions under fluid forces.

On the theoretical side, Katz & Weihs (1978, 1979) also considered the heaving and pitching of a slender airfoil in an inviscid flow. They used a rather different formulation from that presented here. First, they solved their equations using a coordinate transformation, which is somewhat more complicated than the approach used here. Also, they represented the vortex wake as an array of point vortices, rather than the continuous representation here, and consequently used a different expression for the Kutta condition. Their results were limited to three $O(1)$ values of reduced driving frequency. For one frequency, they found an increase in efficiency of flexible foils over rigid foils of up to 20 %. The results given in the present work are new in several respects. First, we give a much more complete characterization of the behaviour throughout the phase space of reduced driving frequency and rigidity, and find a much wider variation of efficiency and thrust. We determine here for the first time optimal parameters for thrust and efficiency. Also new here is the propulsive behaviour at the asymptotic limits of the parameters, together with a theoretical analysis of these results.

Lian *et al.* (2003) have undertaken high-performance computations to simulate the performance of three-dimensional flexible flapping wings and found that passive flexibility can delay the appearance of stall to higher angles of attack. A three-dimensional vortex panel method was used by Liu & Bose (1997) to study the effect of spanwise flexibility on propulsion. It was found to increase propulsive efficiency only under a carefully-controlled time-dependent motion. Miao & Ho (2006) used a dynamic conformal mesh to study a flexible airfoil in a heaving motion at Reynolds numbers of $O(10^4)$. They found that efficiency increased relative to a rigid foil for certain values of the flapping Strouhal number.

The organization of the paper is as follows. Section 2 introduces a model for fully-nonlinear deformations of a flexible body in a high-Reynolds-number flow. This model was used by Alben & Shelley (2008) to study the flag-flapping instability. Section 3 specializes the model to the linearized case of small-amplitude dynamics and in § 4 to periodic dynamics. Section 5 describes the numerical method for solving the linearized, periodic form of the equations. Section 6 gives numerical results in the two-parameter space of dimensionless rigidity and reduced driving frequency. Section 7 analyses the results in the asymptotic regimes of small and large driving frequency (§ 7.1 and § 7.2, respectively). Section 8 compares the optimal parameters identified here with dimensionless parameters from recent studies of insect wings and fish fins. Section 9 collects the main conclusions.

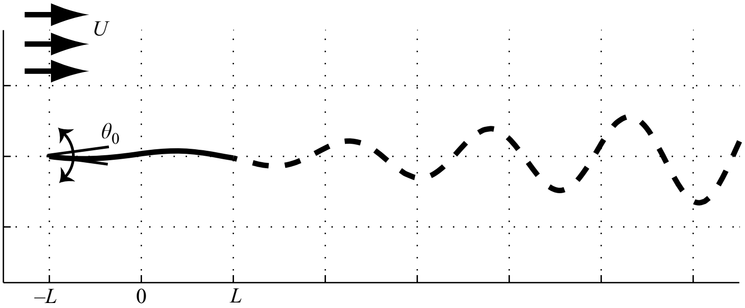

FIGURE 1. A schematic of a flexible fin of length $2L$ pitching at the leading edge with amplitude θ_0 in a steady background flow of speed U. A vortex sheet (dashed line) emanates from the trailing edge.

2. Flexible body vortex sheet model

We model the tail fin of a swimming fish as a slender elastic filament in a two-dimensional inviscid flow (see figure 1). The model fin is an inextensible elastic sheet of length $2L$, mass per unit length ρ_s, and uniform rigidity B, moving under the pressure forces of a surrounding inviscid and incompressible fluid of density (mass per unit area) ρ_f. The fin position is $\zeta(s,t)$, where s is arclength; $-L \leqslant s \leqslant L$. The fin position evolves according to Newton's second law as a geometrically-nonlinear elastica with inertia (Antman 1995):

$$\rho_s \partial_{tt}\zeta(s,t) = \partial_s(T(s,t)\hat{s}) - B\partial_{ss}(\kappa(s,t)\hat{n}) - [p](s,t)\hat{n}. \tag{2.1}$$

Here $T(s,t)$ is a tension force which maintains inextensibility, $\kappa(s,t)$ is the fin curvature, and $[p](s,t)$ is the pressure jump across the fin. We have assumed for simplicity that the rigidity B is uniform, and defer a consideration of the spatial distribution of B to future work.

For simplicity two-dimensional quantities are represented as complex numbers, so that $\zeta(s,t) = x(s,t) + \mathrm{i}y(s,t)$ is the fin position. Here $\hat{s}$ and $\hat{n}$ are complex numbers representing the unit tangent and normal vectors to the fin, respectively. Therefore we have $\hat{s} = \partial_s\zeta = \mathrm{e}^{\mathrm{i}\theta(s,t)}$, where $\theta(s,t)$ is the local tangent angle, and $\hat{n} = \mathrm{i}\mathrm{e}^{\mathrm{i}\theta(s,t)}$. We also define a 'dot product' of two complex numbers $w_1 = a + \mathrm{i}b$ and $w_2 = c + \mathrm{i}d$ to be $w_1 \cdot w_2 = ac + bd$, which is the ordinary dot product of the real vectors (a,b) and (c,d). The curvature is thus $\kappa = -\mathrm{i}\partial_{ss}\zeta \cdot \hat{n}$.

The leading-edge boundary condition for (2.1) is a sinusoidal pitching motion (as if driven by muscles in a fictitious body upstream) with angular frequency ω:

$$\zeta(s=-L,t) = 0; \quad \theta(s=-L,t) = \theta_0\cos(\omega t). \tag{2.2}$$

The kinematics of a tail fin or bird wing are more accurately modelled by including heaving as well as pitching (Lighthill 1969). However, our main interest here is on the thrust as a function of flexibility. We expect the optimal rigidity for pitching to be similar to that for pitching plus heaving, because in both cases the bending rigidity is the key parameter which governs how the leading-edge motion is transmitted to subsequent sections of the body against fluid resistance. In particular, adding heaving does not alter the basic mathematical structure of the equations or the analysis which follows in this work. However, the combination of heaving and pitching should lead to an improvement in performance over pitching alone which is similar to that found in experiments on rigid foils (Triantafyllou *et al.* 1991, 2000). In subsequent work we shall consider combined heaving and pitching.

Free-end boundary conditions, $T=\kappa=\partial_s\kappa=0$, are assumed at the trailing edge ($s=L$). Scaling lengths on L, and time on $2\pi/\omega$, the dimensionless fin equation becomes

$$R_1\partial_{tt}\zeta = \partial_s(T\hat{s}) - R_2\partial_{ss}(\kappa\hat{n}) - [p]\hat{n} \tag{2.3}$$

with dimensionless boundary conditions

$$\zeta(-1,t) = -1; \quad \theta(-1,t) = -\theta_0\cos(2\pi t), \tag{2.4}$$

$$T(1,t) = \kappa(1,t) = \partial_s\kappa(1,t) = 0. \tag{2.5}$$

The dimensionless parameters are:
(*a*) $R_1=\rho_s/\rho_f L$, the dimensionless fin mass,
(*b*) $R_2=B/\rho_f\omega^2L^5$, the dimensionless fin rigidity,
(*c*) θ_0, the dimensionless pitching amplitude.
(*d*) $\Omega=\omega L/U$, the reduced pitching frequency.

The tension is eliminated from (2.3) by integration of the $\hat{s}$-component from $s=1$, using the boundary condition $T(1,t)=0$:

$$T(s,t) = \int_1^s \left(R_1\partial_{tt}\zeta\cdot\hat{s} - \kappa\partial_s(R_2\kappa)\right)\mathrm{d}s'. \tag{2.6}$$

We simplify the problem by observing that a typical fin is composed of bone, collagen, and skin, and has a density similar to that of water. Then the dimensionless mass R_1 is of the order of the fin thickness divided by its length, which is typically $O(10^{-2})$ (Videler 1993). In other words, the inertia of the fin is negligible compared to the inertia of the fluid with which it interacts. Thus for simplicity we set $R_1=0$.

The tail fin is coupled to the flow through the pressure jump in (2.3). The flow is modelled as a two-dimensional inviscid flow, with vorticity in the form of a jump in tangential velocity γ along a continuous curvilinear arc. The arc consists of a 'bound' vortex sheet on the fin, which separates from the trailing edge into a 'free' vortex sheet in the flow (see figure 1). This flow model dates to the early days of airfoil theory (Thwaites 1987), agrees well with experiments (Didden 1979; Pullin & Perry 1980), and has been used more recently by Nitsche & Krasny (1994), Jones (2003), and Pullin & Wang (2004).

The complex conjugate of the flow velocity at any point z in the flow can be calculated in terms of the vortex sheet strength γ by integrating the vorticity in the bound and free sheets against the Biot–Savart kernel (Saffman 1992):

$$u_x(z) - \mathrm{i}u_y(z) = \frac{2\pi}{\Omega} + \frac{1}{2\pi\mathrm{i}}\int_{C_b+C_f} \frac{\gamma(s',t)}{z-\zeta(s',t)}\,\mathrm{d}s'. \tag{2.7}$$

The first term on the right, $2\pi/\Omega$, is the dimensionless flow velocity at infinity, according to the non-dimensionalization used in (2.3). Here C_b is the contour representing the fin ($-1\leqslant s'\leqslant 1$) and C_f is the contour representing the free sheet ($1\leqslant s'\leqslant s_{\max}$). We can express the average of the flow velocities w on the two sides of any point $\zeta(s,t)$ on C_b or C_f by taking the average of the limits of (2.7) as z approaches $\zeta(s,t)$ from above and below the countours:

$$\bar{w}(s,t) = \frac{2\pi}{\Omega} + \frac{1}{2\pi\mathrm{i}}\,⨍_{-1}^{1} \frac{\gamma(s',t)}{\zeta(s,t)-\zeta(s',t)}\,\mathrm{d}s' + b(s,t), \tag{2.8}$$

$$b(s,t) = \frac{1}{2\pi\mathrm{i}}\,⨍_{1}^{s_{\max}} \frac{\gamma(s',t)}{\zeta(s,t)-\zeta(s',t)}\,\mathrm{d}s'. \tag{2.9}$$

In (2.8), $\bar{w}$ is the complex conjugate of w, and the integral is of principal-value type. On the free vortex sheet C_f, it can be shown that points $\zeta(s)$ move with velocity w

(Saffman 1992, p. 31). This gives the Birkhoff–Rott equation for the evolution of the free vortex sheet:

$$\frac{\partial \bar{\zeta}(s,t)}{\partial t}(s,t) = \frac{2\pi}{\Omega}\hat{e}_x + \frac{1}{2\pi \mathrm{i}} P_{C_b+C_f} \; \frac{\gamma(s',t)}{\zeta(s,t)-\zeta(s',t)}\,\mathrm{d}s', \qquad \zeta(s,t) \in C_f. \tag{2.10}$$

We apply (2.8) also to $\zeta(s)$ on the fin, to express the kinematic condition that fluid does not penetrate the fin on either side. In other words, the component of the fin velocity normal to the fin equals the normal component of w:

$$\hat{n}\cdot\partial_t\zeta(s,t) = \hat{n}\cdot w(s,t), \qquad \zeta(s,t)\in C_b, \tag{2.11}$$

$$\hat{n}\cdot\partial_t\zeta(s,t) = \hat{n}\cdot\left(\frac{2\pi}{\Omega}\hat{e}_x + \frac{1}{2\pi\mathrm{i}}\fint_{-1}^{1}\frac{\gamma(s',t)\,\mathrm{d}s'}{\zeta(s)-\zeta(s')}\right) + \hat{n}\cdot b(s,t),\ \ \zeta(s,t)\in C_b. \tag{2.12}$$

When the left-hand side of (2.12) and $b(s,t)$ are known, the general solution $\gamma(s,t)$ has inverse-square-root singularities at $s=\pm 1$ (Muskhelishvili 1953). If we define $v(s,t)$, the bounded part of $\gamma(s,t)$, by

$$\gamma(s,t) = \frac{v(s,t)}{\sqrt{1-s^2}}, \tag{2.13}$$

the kinematic condition becomes

$$\hat{n}\cdot\partial_t\zeta(s,t) = \hat{n}\cdot\left(\frac{2\pi}{\Omega}\hat{e}_x + \frac{1}{2\pi\mathrm{i}}\fint_{-1}^{1}\frac{v(s',t)\,\mathrm{d}s'}{\sqrt{1-s'^2}(\zeta(s)-\zeta(s'))}\right) + \hat{n}\cdot b(s,t), \quad \zeta(s,t)\in C_b. \tag{2.14}$$

We can rewrite $b(s,t)$ in a more convenient form. The free vortex sheet consists of a line of fluid particles which are continually advected away from the trailing end of the fin, for $t \geqslant 0$. Following Jones (2003), we define the circulation as the integral of γ over the free sheet:

$$\Gamma(s,t) = \int_{s_{\max}}^{s}\gamma(s',t)\,\mathrm{d}s', \quad -1 < s < s_{\max}. \tag{2.15}$$

We denote the total circulation in the free sheet $\Gamma_{+}(t) = \int_{s_{\max}}^{1}\gamma\,\mathrm{d}s'$. According to the Helmholtz laws for vorticity conservation in two-dimensional flows, specialized to a vortex sheet, $\Gamma(s,t)$ is conserved on fluid particles (Saffman 1992, p. 30):

$$\frac{\mathrm{d}}{\mathrm{d}t}\Gamma(s,t) = 0, \quad s \in C_f. \tag{2.16}$$

where the time derivative is a material derivative, the rate of change following a fluid particle, which moves according to (2.10). Thus each fluid particle in C_f carries the value of circulation $\Gamma(s,t) = \Gamma(1,t^*)$ it has at the time t^* when it is 'born' at the trailing edge of the fin. We can reparametrize $b(s,t)$ in (2.9) by circulation Γ using $\gamma\,\mathrm{d}s = d\Gamma$:

$$b(s,t) = -\fint_{0}^{\Gamma_{+}(t)}\frac{\mathrm{d}\Lambda'}{\zeta(s,t)-\zeta(\Lambda',t)}. \tag{2.17}$$

The instantaneous total circulation in the free sheet, $\Gamma_{+}(t)$, is determined by the Kutta condition, which states that at each time t the fluid velocity at the trailing edge $s=1$ is finite. In particular, γ, which is also the tangential component of the jump in fluid velocity across the fin must be finite at the trailing edge. Using (2.13), the Kutta condition becomes

$$v(1,t)=0. \tag{2.18}$$

At each time t, (2.18) is a constraint which we use to determine $\Gamma_+(t)$, as described below.

One can relate the pressure jump across the fin $[p]$ to the vortex sheet strength along the fin by a version of the unsteady Bernoulli equation. One writes the Euler equations for fluid velocities at points above and below the fin, and takes the limit that the points approach each other from opposite sides of the fin (see Saffman 1992; Jones 2003). The difference of these equations is an evolution equation for the difference of the fluid velocities, which is $\gamma\,\hat{s}$ (the normal component is zero by the no-penetration condition on either side of the fin). The evolution equation for the vortex sheet strength γ is (Jones 2003):

$$\gamma_t+\partial_s((\mu-\tau)\gamma)=\partial_s[p], \tag{2.19}$$

where τ is the tangential component of the fin velocity and $\mu(s,t)$ is the tangential component of the average fluid velocity:

$$\tau(s,t)=\partial_t\zeta(s,t)\cdot\hat{s};\quad \mu=w(s,t)\cdot\hat{s}. \tag{2.20}$$

The pressure jump across the free sheet is zero, which yields the boundary condition for (2.19),

$$[p]\,|_{s=1}=0. \tag{2.21}$$

We integrate (2.19) along C_b to determine $[p]\,(s,t)$ on the fin $-1<s<1$.

We present here the full system of unknowns and corresponding equations:

$$\left.\begin{aligned}\zeta(s,t),s\in C_b,-1\leqslant s\leqslant 1 &: (2.3),\\ v(s,t),s\in C_b &: (2.14),\\ [p]\,(s,t),s\in C_b &: (2.19)\text{ and }(2.13),\\ \zeta(s,t),s\in C_f,1\leqslant s\leqslant s_{\max} &: (2.10),\\ \Gamma(s,t)=\Gamma(1,t^*),s\in C_f &: (2.18).\end{aligned}\right\} \tag{2.22}$$

Because the fin is nearly aligned with the flow, we neglect separation upstream of the trailing edge, and allow the flow velocity and pressure to diverge as the inverse square root of distance from the leading edge. The divergent pressure creates a finite leading-edge suction on the body which is a reasonable model for the force in the actual flow (Saffman 1992), and is a standard component of classical models for flows past slender airfoils (Thwaites 1987).

The main quantities of interest are the instantaneous force on the fin Q, the input power P_{in} (the rate of work done per unit time at the leading edge) and the output power P_{out}. These are

$$Q=-\frac{\pi}{8}v(-1)^2\hat{s}+\int_{-1}^{1}-[p]\hat{n}\,\mathrm{d}s, \tag{2.23}$$

$$P_{in}=-R_2\kappa\frac{\partial\theta}{\partial t}\bigg|_{s=-1}, \tag{2.24}$$

$$P_{out}=\frac{\pi^2}{4\Omega}v(-1)^2+\frac{2\pi}{\Omega}\int_{-1}^{1}[p]\hat{n}\cdot\hat{e}_x\,\mathrm{d}s. \tag{2.25}$$

The first term on the right-hand side of (2.23) is a suction force due to the inverse-square-root flow singularity at the leading edge. This is the limit of the suction force on a leading edge of small but finite radius of curvature, in the limit that the radius tends to zero (i.e. the body becomes sharp-edged) (Saffman 1992). Equation (2.24) is the rate of work done to create the pitching motion, equal to the moment applied at the leading edge $-R_2\kappa$ times the angular velocity there. The output power is defined as the rate of work done per unit time by thrust forces on the fin, which is the thrust force times the velocity of the fluid stream $2\pi/\Omega$. This form of P_{out} was used by Lighthill (1960) and many others in the 'Froude efficiency.'

3. Small-amplitude linearization

The general system of (2.22) becomes more amenable to analysis in the regime of small pitching amplitude, $\theta_0 \ll 1$. We specialize the system (2.22) to this limit by expanding all quantities to linear order in θ_0. First we linearize $\hat{s}$ and $\hat{n}$. We have

$$\hat{s} = \frac{\partial x}{\partial s} + \mathrm{i}\frac{\partial y}{\partial s} = \mathrm{e}^{\mathrm{i}\theta} = 1 + \mathrm{i}\theta + O\left(\theta_0^2\right), \tag{3.1}$$

$$\hat{n} = \mathrm{i}\mathrm{e}^{\mathrm{i}\theta} = \mathrm{i} - \theta + O\left(\theta_0^2\right). \tag{3.2}$$

Since $\partial x/\partial s \sim 1 + O(\theta_0^2)$, all s-derivatives in (2.3) equal x-derivatives to linear order. Thus,

$$\kappa\hat{n} = \mathrm{i}\frac{\partial^2 y}{\partial x^2} + O\left(\theta_0^2\right). \tag{3.3}$$

Recalling that $R_1 = 0$, (2.6) shows that $T \leqslant O(\theta_0^2)$. Thus the tension term drops out of (2.3) at linear order. The imaginary part of the linearized beam equation with $R_1 = 0$ is thus

$$0 = -R_2\partial_x^4 y - [p]. \tag{3.4}$$

The boundary conditions are

$$y|_{x=-1} = 0, \quad \partial_x y|_{x=-1} = \theta_0 \cos 2\pi t; \tag{3.5}$$

$$\partial_{xx} y|_{x=1} = \partial_{xxx} y|_{x=1} = 0. \tag{3.6}$$

Next we linearize (2.14). Using (3.1), (3.2) and the boundary conditions (2.4),

$$\partial_t \zeta = \partial_t \zeta|_{s=-1} + \partial_t \int_{-1}^{s} (\partial_s x + \mathrm{i}\partial_s y)\, \mathrm{d}s' = \mathrm{i}\partial_t y + O\left(\theta_0^2\right). \tag{3.7}$$

Thus $\partial_t\zeta \cdot \hat{n} = \partial_t y + O(\theta_0^2) = O(\theta_0)$. Using (3.2), the first term on the right-hand side of (2.14) is

$$\hat{n} \cdot \left(\frac{2\pi}{\Omega}\hat{e}_x\right) = -\frac{2\pi}{\Omega}\partial_x y + O\left(\theta_0^2\right), \tag{3.8}$$

which is also $O(\theta_0)$. The kernels (i.e. the terms multiplying γ) in the principal-value integral and in $b(s,t)$, defined in (2.8), (2.9) are $O(1)$. Thus the functions γ they multiply are $O(\theta_0)$ to balance the other $O(\theta_0)$ terms in the equations.

We can linearize the kernels in (2.8), (2.9) by retaining only the $O(1)$ terms in the kernels. On the fin, reasoning similar to that in (3.7) shows that $\zeta(s,t) = s + O(\theta_0)$. Thus,

$$\frac{1}{\zeta(s) - \zeta(s')} = \frac{1}{s - s'} + O(\theta_0), \quad -1 < s < 1. \tag{3.9}$$

The left-hand side of (2.10) equals the constant background flow velocity $2\pi/\Omega$ at zeroth order. Thus at zeroth order the position of the free vortex sheet is the semi-infinite line $1 < x < \infty$, $y = 0$. We assume the fin has been oscillating for a long time, and thus take ∞ as the upper limit in x.

We assume all quantities have the same frequency as the pitching at the leading edge (2.4). This is supported by simulations of the initial value problem, which are very nearly periodic for small θ_0 (see the Appendix). In particular, the total circulation in the sheet is periodic, $\Gamma(x=1,t)=\mathrm{Re}\left(\Gamma_0 \mathrm{e}^{\mathrm{i}2\pi t}\right)$. Γ is conserved on material points of the sheet which are advected downstream at constant velocity $(2\pi/\Omega)\hat{e}_x$. Thus the material point at location $x \geqslant 1$ at time t was at location $x=1$ at time $t-\Omega(x-1)/(2\pi)$. Hence, the circulation on the x-axis is a travelling wave:

$$\Gamma(x,t) = \mathrm{Re}\left(\Gamma_0 \mathrm{e}^{-\mathrm{i}\Omega(x-1)}\mathrm{e}^{\mathrm{i}2\pi t}\right), \tag{3.10}$$

$$\gamma(x,t) = \partial_x \Gamma(x,t) = \mathrm{Re}\left(-\mathrm{i}\Omega\Gamma_0 \mathrm{e}^{-\mathrm{i}\Omega(x-1)}\mathrm{e}^{\mathrm{i}2\pi t}\right). \tag{3.11}$$

Thus, $b(s,t)$ in (2.9) becomes

$$b(x,t) = \frac{1}{2\pi}\mathrm{Re}\left(-\Omega\Gamma_0 ⨍_1^{\infty} \frac{\mathrm{e}^{-\mathrm{i}\Omega(x'-1)}}{x-x'}\,\mathrm{d}x' \mathrm{e}^{\mathrm{i}2\pi t}\right), \tag{3.12}$$

and the linearized form of (2.14) is:

$$\partial_t y(x,t) + \frac{2\pi}{\Omega}\partial_x y(x,t) = \frac{1}{2\pi} ⨍_{-1}^{1} \frac{v(x',t)\,\mathrm{d}x'}{\sqrt{1-x'^2}(x-x')} + b(x,t), \quad -1 < x < 1. \tag{3.13}$$

We linearize $[p]$ by linearizing (2.19), as follows. Using (2.20) and (2.8), $\mu = 2\pi/\Omega + O(\theta_0)$. Using reasoning similar to that in (3.7), $\tau = \partial_t \zeta \cdot \hat{s} = O(\theta_0)$. Thus the linearized form of (2.19) is

$$\gamma_t + \frac{2\pi}{\Omega}\partial_x \gamma = \partial_x [p], \tag{3.14}$$

which shows that $[p] = O(\theta_0)$, consistent with the other term in (3.4).

Finally, the linearized version of the Kutta condition (2.18) is unchanged.

We present here the full system of unknowns and corresponding linearized equations:

$$\left.\begin{aligned} &y(x), -1 \leqslant x \leqslant 1 : (3.4), \\ &v(x), -1 \leqslant x \leqslant 1 : (3.13), \\ &[p](x), -1 \leqslant x \leqslant 1 : (3.14), \\ &\Gamma_0 : (2.18). \end{aligned}\right\} \tag{3.15}$$

Because the position of the free sheet is known, (2.10) in system (2.22) is no longer needed.

4. Periodic case

As stated previously in deriving the linearized form of the free vortex sheet, (3.10), we assume a periodic Ansatz for all quantities, including

$$\left.\begin{aligned} &y(x,t) = \mathrm{Re}(Y(x)\mathrm{e}^{2\pi\mathrm{i}t});\ v(x,t) = \mathrm{Re}(V(x)\mathrm{e}^{2\pi\mathrm{i}t});\ \gamma(x,t) = \mathrm{Re}(G(x)\mathrm{e}^{2\pi\mathrm{i}t}); \\ &[p](x,t) = \mathrm{Re}(P(x)\mathrm{e}^{2\pi\mathrm{i}t});\ \Gamma(x=1,t) = \mathrm{Re}(\Gamma_0\mathrm{e}^{2\pi\mathrm{i}t}). \end{aligned}\right\} \tag{4.1}$$

In this section we write the system of equations for the purely spatial terms on the right sides of (4.1). Equation (3.4) yields

$$0 = -R_2 \partial_x^4 Y - P. \tag{4.2}$$

The boundary conditions are

$$Y|_{x=-1} = 0,\ \partial_x Y|_{x=-1} = \theta_0; \tag{4.3}$$

$$\partial_{xx} Y|_{x=1} = \partial_{xxx} Y|_{x=1} = 0. \tag{4.4}$$

Equation (3.14) yields

$$2\pi \mathrm{i} G(x) + \frac{2\pi}{\Omega}\partial_x G(x) = \partial_x P(x) \tag{4.5}$$

with boundary condition

$$P|_{x=1} = 0. \tag{4.6}$$

The linearized kinematic condition (3.13) yields

$$2\pi \mathrm{i} Y(x) + \frac{2\pi}{\Omega}\partial_x Y(x) = \frac{1}{2\pi} ⨍_{-1}^{1} \frac{V(x')\,\mathrm{d}x'}{\sqrt{1-x'^2}(x-x')} + B(x), \quad -1 < x < 1. \tag{4.7}$$

$$B(x) = -\frac{\Omega \Gamma_0}{2\pi} \int_1^\infty \frac{\mathrm{e}^{-\mathrm{i}\Omega(x'-1)}}{x-x'}\,\mathrm{d}x', \tag{4.8}$$

$$B(x) = \Gamma_0 E(x). \tag{4.9}$$

We have defined the function in $B(x)$ which Γ_0 multiplies as $E(x)$, an exponential integral function.

5. Numerical method

We now give our numerical method for the solution of the spatial terms in the periodic form of system (3.15), which consists of (4.2), (4.5), (4.7) and the Kutta condition (2.18) (i.e. $V(x=1)=0$). Although the system is linear, the matrix is somewhat complicated to set up. Thus we solve it numerically using an iterative method known as Broyden's method (Ralston & Rabinowitz 2001), which is somewhat simpler to code, and which converges rapidly since the system is linear. We write our system of (4.2), (4.7), (4.5) and (2.18) in the form

$$\boldsymbol{F}(\boldsymbol{a}) = 0. \tag{5.1}$$

The unknowns $\boldsymbol{a}$ are values of V (defined in (4.1)) and $\partial_{xx} Y$ on $m+1$ Chebyshev–Lobatto nodes in $-1 < x < 1$, and the total circulation Γ_0:

$$a_j = V(x_j), \quad j = 1, \ldots, m+1, \tag{5.2}$$

$$a_{j+m+1} = \partial_{xx} Y(x_j), \quad j = 1, \ldots, m+1, \tag{5.3}$$

$$a_{2m+3} = \Gamma_0, \tag{5.4}$$

$$x_j = -\cos (j-1)\pi/m, \quad j = 1, \ldots, m+1. \tag{5.5}$$

The values $\boldsymbol{F}$ in the corresponding $2m+3$ linear equations are computed as follows. We start by integrating $\partial_{xx} Y(x_j)$ twice to obtain the body deflection $Y(x_j)$ using the 'clamp' boundary conditions (4.3).

We compute the integral in (4.8) prior to beginning the iterative process. During the iterative process, we multiply the pre-computed integral by Γ_0 to obtain $B(x_j)$.

Equation (4.7) can be solved for V using a Chebyshev expansion. We define

$$f(x) = -B(x) + 2\pi \mathrm{i} Y(x) + \frac{2\pi}{\Omega} \partial_x Y(x) \tag{5.6}$$

and approximate f by a finite Chebyshev series, which converges rapidly for smooth functions:

$$f(x) = \sum_{k=0}^{n} f_k \cos(k\phi), \quad x = \cos(\phi). \tag{5.7}$$

The solution V is (Mason & Handscomb 2003)

$$V(x) = 2\sum_{k=1}^{n} f_k \sin(k\phi)\sin(\phi) - f_1 - 2f_0\cos(\phi) + C. \tag{5.8}$$

The constant C is determined by the conservation of circulation (Kelvin's Theorem) for a flow started from rest:

$$\int_{-1}^{1} \frac{V(x)}{\sqrt{1-x^2}} e^{2\pi \mathrm{i} t}\, \mathrm{d}x + \Gamma_0 e^{2\pi \mathrm{i} t} = 0 \Rightarrow C = \frac{\Gamma_0}{\pi}. \tag{5.9}$$

Using (5.8) we can write the Kutta condition (2.18) as

$$-f_1 - 2f_0 + \frac{\Gamma_0}{\pi} = 0. \tag{5.10}$$

Having computed each of the quantities in (4.7), we now place it in our system of equations:

$$F_i(\boldsymbol{a}) = V(x_i) - 2\sum_{j=1}^{n} f_j \sin(j\phi_i)\sin(\phi_i) + f_1 + 2f_0\cos(\phi_i) - \frac{\Gamma_0}{\pi}, \quad i = 1, \ldots, m+1. \tag{5.11}$$

Next, we form the terms in the beam equation (4.2). We compute P by integrating (4.5) with boundary condition (4.6). The inverse-square-root singularity in γ and G at the leading edge $x = -1$ also appears in P, and thus in $\partial_{xxxx} Y$ through (4.2). This does not pose a significant problem, since we do not evaluate (4.2) at the leading edge. We adopt the standard approach of including in this system of equations (4.2) evaluated on the interior nodes only. Since (4.2) is second-order in $\partial_{xx} Y$, we replace the equations on the two boundary nodes x_1, x_{m+1} with the two boundary conditions $\partial_{xx} Y(x_{m+1}) = \partial_{xxx} Y(x_{m+1}) = 0$. The equations we add to our system of nonlinear equations corresponding to the beam equation are then

$$F_{j+m}(\boldsymbol{a}) = -R_2 D_x^2(\partial_{xx} Y(x_j)) + -P(x_j), \quad j = 2, \ldots, m, \tag{5.12}$$

$$F_{2m+1}(\boldsymbol{a}) = \partial_{xx} Y(x_{m+1}), \tag{5.13}$$

$$F_{2m+2}(\boldsymbol{a}) = D_x^1 \partial_{xx} Y(x_{m+1}). \tag{5.14}$$

Here D_x^1 and D_x^2 are the discrete differentiation matrices of first and second order on Chebyshev–Lobatto nodes. They are dense matrices, but because the number of nodes $m+1$ is typically small ($\approx O(10^2)$), multiplication by these matrices is computationally inexpensive. A uniform discretization would allow sparse differentiation matrices, but then it would need to interpolate from data on a uniform mesh to data on a Chebyshev mesh, which increases the condition number of the Jacobian matrix $\partial F_j/\partial a_i$, slowing convergence. The last equation in our nonlinear system is the Kutta condition (5.10):

$$F_{2m+3}(\boldsymbol{a}) = -f_1 - 2f_0 + \frac{\Gamma_0}{\pi}. \tag{5.15}$$

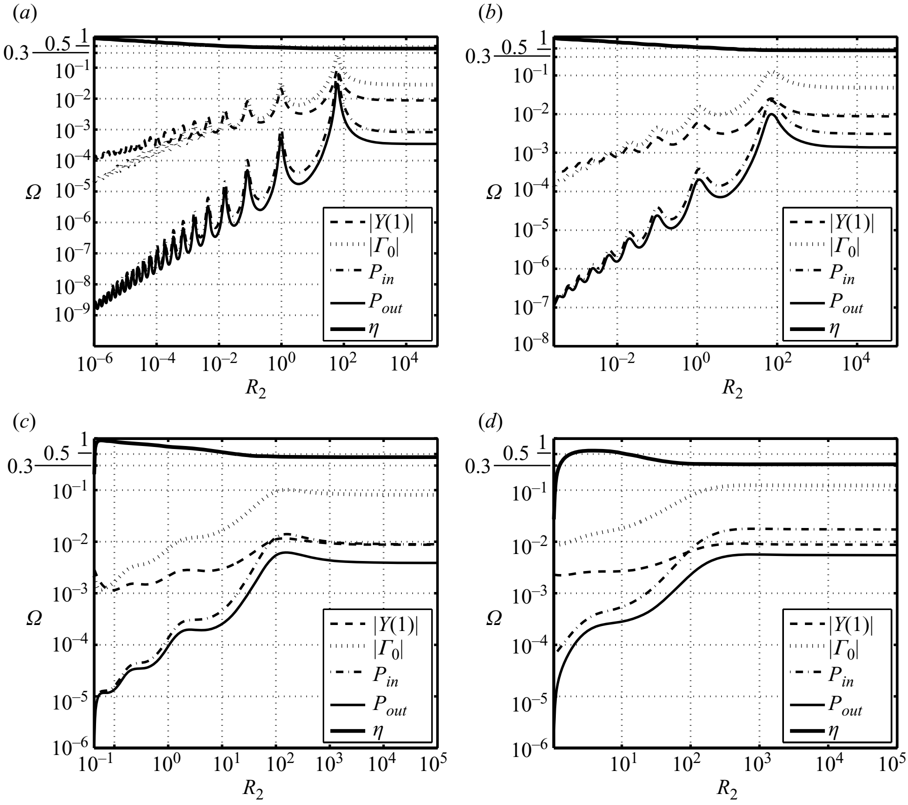

FIGURE 2. For the flexible fin pitching at the leading edge in the linearized regime ($\theta_0 = \pi/720$): time-averaged output power $\langle P_{out}\rangle$, time-averaged input power $\langle P_{in}\rangle$, efficiency $\eta = \langle P_{out}\rangle / \langle P_{in}\rangle$, and maximum tail deflection $|Y(1)|$ and circulation $|\Gamma_0|$, over a period. All quantities are plotted versus bending rigidity R_2, for four values of Ω: 25 (*a*), 6 (*b*), 2 (*c*) and 1 (*d*).

Having computed the solution $\boldsymbol{a}$ at each time step, we can compute the time-averaged force, input power and output power. Inserting the linearized periodic expressions (4.1) into (2.23)–(2.25), and taking the average over one period, we obtain

$$\langle Q\rangle = -\frac{\pi}{16}|V(-1)|^2 + \int_{-1}^{1} -P(x)\partial_x Y(x)\,\mathrm{d}x, \tag{5.16}$$

$$\langle P_{in}\rangle = -\frac{R_2}{2}\mathrm{Im}(\partial_{xx}Y)|_{x=-1}2\pi\theta_0, \tag{5.17}$$

$$\langle P_{out}\rangle = \frac{\pi^2}{8\Omega}|V(-1)|^2 + \int_{-1}^{1} -P\partial_x Y(x)\,\mathrm{d}x. \tag{5.18}$$

6. Results

We now examine the fin solutions in the limit $\theta_0 \ll 1$ as functions of the two key parameters: flapping frequency Ω and rigidity R_2. In figure 2, we set $\theta_0 = \pi/720$ and plot the quantities in (5.17)–(5.18) for four values of Ω, decreasing to unity, and for many decades of R_2. In addition, we have plotted the tail end deflection $|Y(1)|$, and the magnitude of the circulation shed by the fin, $|\Gamma_0|$. In figure 2(*a*) ($\Omega = 25$), we find a series of sharp resonance-like peaks in the response as a function of R_2, which reach

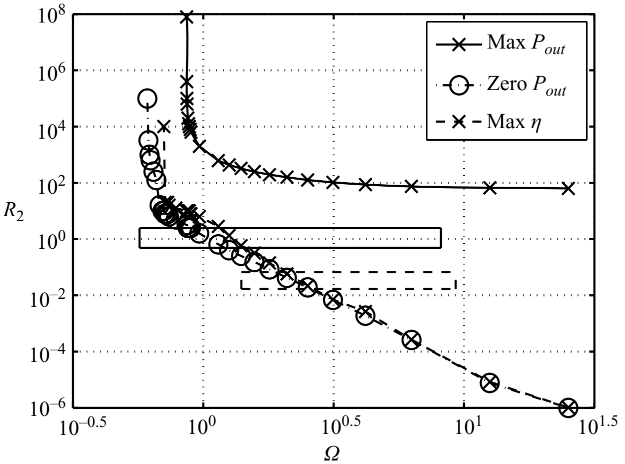

FIGURE 3. For the flexible fin pitching at the leading edge in the linearized regime ($\theta_0 = \pi/720$): The values of rigidity R_2 corresponding to maximum time-averaged output power $\langle P_{out}\rangle$, maximum efficiency $\eta = \langle P_{out}\rangle/\langle P_{in}\rangle$ and zero output power, as a function of reduced pitching frequency Ω. Also plotted are a range of typical values from studies of the hawkmoth Manduca Sexta (solid box), and the bluegill sunfish Lepomis Macrochirus (dashed box). See § 8 for details on these studies.

plateaux for $R_2 \gtrsim 10^3$, where the rigid-plate solution is achieved. In addition, we find the following power-law scalings of the peaks for $R_2 < O(10^2)$:

$$P_{in} \sim R_2^{0.95},\ P_{out} \sim R_2^{0.88},\ |Y(1)| \sim R_2^{0.35},\ |\Gamma_0| \sim R_2^{0.55}. \tag{6.1}$$

The efficiency decreases from near unity for $R_2 \ll 1$ to 41% for $R_2 \gg 1$ in figure 2(*a*). In figure 2(*b*, *c*, *d*) we decrease Ω to 6, 2 and 1, respectively, and plot the same quantities. We again find a series of peaks, though as Ω decreases, the peak amplitudes decrease, and half-widths increase, characteristic of increased damping in a resonant system. We note, however, that there is no energy dissipation in this system, unlike the classical damped, driven harmonic oscillator. However, mathematically our system is analogous to a damped resonant system, as explained in § 7.

We have set the lower limit of R_2 in these plots to the values below which the thrust power $\langle P_{out}\rangle$ becomes negative (i.e. thrust becomes drag). We shall comment on the behaviour below this transition subsequently. Near these lower limits of R_2 for thrust, the efficiency η peaks and then decreases sharply to zero. The peak values of η decrease with decreasing Ω.

Similarities between all four panels of figure 2 are that the power-law scalings of the peaks are the same, and that the transition to the rigid-plate solution occurs at approximately the same value of R_2.

It can be seen that the peaks in $\langle P_{out}\rangle$ coincide with peaks in the amplitude at the trailing edge of the fin. These coincide also with the peaks in amplitude at other locations along the fin, although with different temporal phases at different locations. In a more approximate localized theory of fluid forces on a body with a prescribed travelling-wave motion, Lighthill (1960) predicted a strong dependence of thrust on the trailing edge deflection in particular.

We have scanned over a wide range of Ω, and at each Ω identified the values of R_2 which correspond to the maximum $\langle P_{out}\rangle$, maximum efficiency $\langle P_{out}\rangle / \langle P_{in}\rangle$, and the thrust–drag transition (zero $\langle P_{out}\rangle$). These values are plotted in figure 3. At

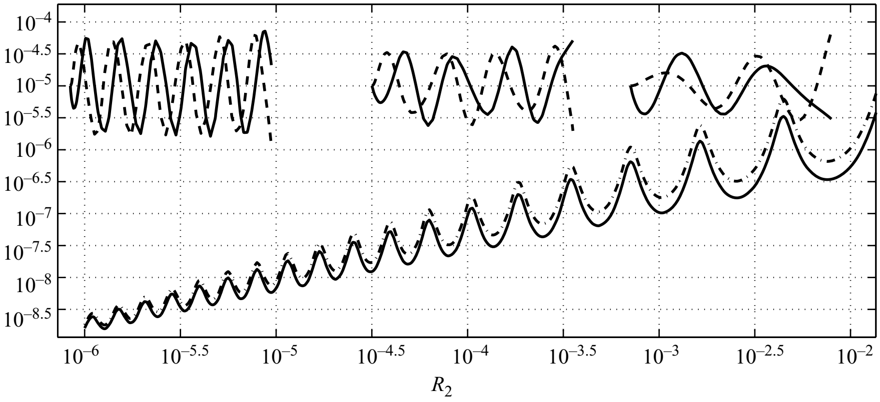

FIGURE 4. The sin(t)- and cos(t)-components of the fin shapes for $R_2 \ll 1$, at $\Omega = 25$. The shapes are arranged so that their horizontal midpoint is at the corresponding value of R_2. Upper curves: solid line, cos(t)-component; dashed line, sin(t)-component. Lower curves: solid line, time-averaged output power; dot-dashed line, time-averaged input power.

large reduced frequencies, the optimal R_2 for thrust is approximately 60. At smaller frequencies, the optimal R_2 for thrust tends abruptly to ∞ at $\Omega = 0.27$, yielding the rigid plate solution. As Ω approaches this value from above, the uppermost peak in the plots of figure 2 becomes shallower and shallower, and finally transitions to a monotonic rise with R_2.

For large frequencies Ω, the values of R_2 for maximum efficiency drop sharply, as $R_2 \sim \Omega^{-5}$. At lower Ω the maximum efficiency R_2 increases sharply to ∞ at $\Omega = 0.22$. The values of R_2 corresponding to the thrust–drag transition also increase to ∞. In other words, there is a lower bound on Ω below which no thrust can be generated by a flapping body of any rigidity. As studies on rigid bodies have found, a body must flap at a certain speed relative to the speed of the oncoming stream to produce thrust (Vandenberghe *et al.* 2004; Alben & Shelley 2005; Godoy-Diana, Aider & Wesfreid 2008). Scaling arguments have predicted high efficiency in the linear regime (Sparenberg 2002) and here we find that efficiency is near one when thrust tends to zero. In other words, efficiency is high when circulation $|\Gamma_0|$ is small, so little energy is put into the wake.

We have focused so far on integral measures of the fin behaviour. We can understand the structure of the solution in more detail by examining the spatial behaviour of solutions on the fin. We begin by examining the fin shapes corresponding to the peaks in the small-R_2 power-law regime in figure 2(a). In figure 4 we superpose the sin($2\pi t$)- and cos($2\pi t$)-components of three fin shapes above the plots for input and output power. The values of R_2 for these shapes are directly below their horizontal midpoints. All of the shapes have been rescaled to have a common amplitude. The most notable feature is a decrease in wavelength of the solutions with decreasing R_2. Such behaviour is typical of resonant solutions to the beam equation with decreasing rigidity.

In figure 5 we plot several fin shapes between peaks in R_2 for a higher range of R_2 in figure 2, near the four highest peaks in response. All of the shapes have been rescaled to a common amplitude. As the shapes move from peaks to troughs the relative balance in fin response shifts from the sin($2\pi t$)-component at the peaks to the cos($2\pi t$)-component – the driving component – at the troughs. At the highest peak we see that the optimal-thrust shape has curvature of a single sign, concentrated at the leading edge.

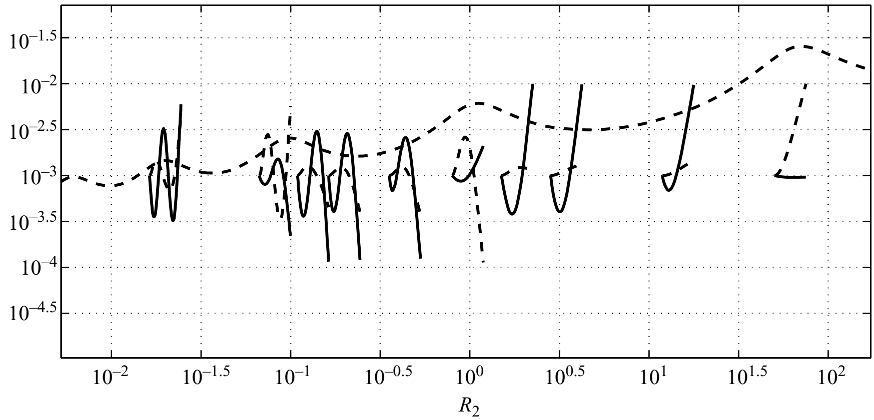

FIGURE 5. The $\sin(2\pi t)$- and $\cos(2\pi t)$-components (dashed and solid short lines respectively) of the fin shapes for maxima and minima of thrust versus R_2, at $\Omega = 25$. The shapes are arranged so that their horizontal midpoint is at the corresponding value of R_2. The dashed curve running across the figure is the time-averaged output power.

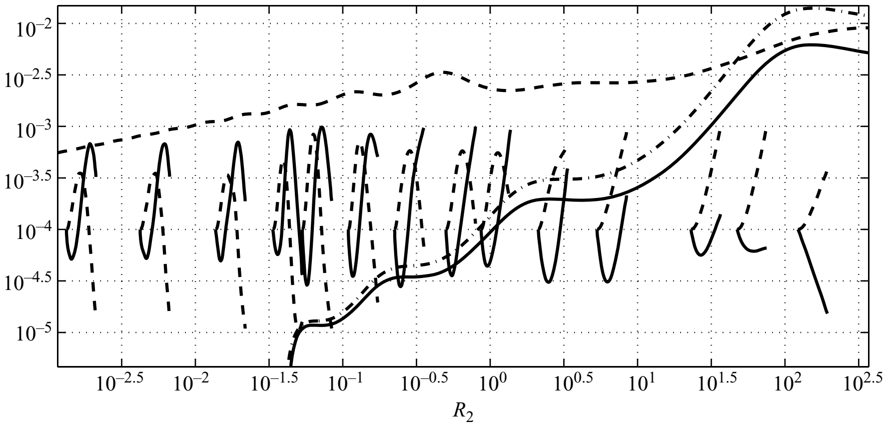

FIGURE 6. The $\sin(2\pi t)$- and $\cos(2\pi t)$-components (dashed and solid short lines respectively) of the fin shapes for $\Omega = 2$. The shapes are arranged so that their horizontal midpoint is at the corresponding value of R_2. The long curves are: solid, time-averaged output power; dot-dashed, time-averaged input power; dashed, peak deflection at the trailing edge of the fin over a flapping period.

In figure 6 we plot fin shapes corresponding to the smaller value of $\Omega = 2$, with results given in figure 2(*c*). The peaks no longer correspond as clearly to dominance of the $\sin(2\pi t)$ components of response. We show also fin shapes for R_2 below the thrust-drag transition $R_2 \approx 10^{-1.3}$. Apart from a region near the leading edge, we find convergence to a particular fin trajectory, apart from a scaling of overall amplitude as $R_2^{1/3}$ (In figure 6 the shapes have been re-scaled to a common amplitude.) This power law is close to the power law $|Y(1)| \sim R_2^{0.35}$ above the thrust–drag transition. However the solutions are quite different on either side of the transition. As R_2 decreases from ∞ in figure 6, the wavelengths of the shapes decrease until the thrust–drag transition. As R_2 decreases below this transition, solutions have a common shape apart from the scaling of overall amplitude. This change corresponds to a change in the dominant balance in the fluid–body equation, which gives rise to a similarity solution as described in § 7.1.

In summary, the main observations of this section are

1. The appearance of resonant-like peaks in response at particular values of fin rigidity R_2.
2. The damping of the peaks with decrease of Ω.
3. The power-law scalings of response with rigidity R_2.
4. The appearance of shapes with characteristic wavelengths which decrease with R_2.
5. The scalings of the zero-thrust and maximum efficiency values of R_2 at large Ω.
6. The different phase behaviour of solutions at peaks and troughs in response.
7. The approach of efficiency to one for small R_2.

We shall now attempt to understand the first four of these observations by an approximate analysis of solutions to the equations. Along the way we shall present the solutions in the limit of small Ω and small R_2, which are self-similar.

7. Analysis

Here we rationalize some of the main observations in the previous section by examining the dominant balances in the system of equations in asymptotic limits of R_2 and Ω. First, we use (5.10), (5.6), (4.8) and (4.9) to express Γ_0 explicitly in terms of Y:

$$\Gamma_0 = \pi \int_{-1}^{1} \sqrt{\frac{1+x'}{1-x'}} \left(-B(x') + 2\pi \mathrm{i} Y(x') + \frac{2\pi}{\Omega} \partial_{x'} Y(x') \right) \mathrm{d}x' \tag{7.1}$$

$$= J\left(2\pi \mathrm{i} Y(x) + \frac{2\pi}{\Omega} \partial_x Y(x) \right). \tag{7.2}$$

$$J(\cdot) = \frac{\displaystyle\int_{-1}^{1} \sqrt{\frac{1+x'}{1-x'}} (\cdot)\, \mathrm{d}x'}{1 + \displaystyle\int_{-1}^{1} \sqrt{\frac{1+x'}{1-x'}} E(x')\, \mathrm{d}x'}. \tag{7.3}$$

This shows that Γ_0 is a weighted integral of the flow velocity normal to the fin, divided by a fixed function. We denote this functional by J.

It is helpful to combine the system of equations (4.2), (4.5) and (4.7) into a single equation in terms of Y. Combining (4.2) and (4.5) gives

$$0 = -R_2 \partial_x^5 Y - 2\pi \mathrm{i} G(x) - \frac{2\pi}{\Omega} \partial_x G(x), \tag{7.4}$$

where we have used the uniformity of R_2. We can write (4.7) as

$$2\pi \mathrm{i} Y(x) + \frac{2\pi}{\Omega} \partial_x Y(x) = \frac{1}{2} \mathscr{H}(G(x)) + E(x) J\left(2\pi \mathrm{i} Y(x) + \frac{2\pi}{\Omega} \partial_x Y(x) \right) \tag{7.5}$$

where $\mathscr{H}(G(x))$ is the finite Hilbert transform,

$$\mathscr{H}(G(x)) = \frac{1}{\pi} \fint_{-1}^{1} \frac{G(x')}{(x-x')}\, \mathrm{d}x'. \tag{7.6}$$

We invert $\mathscr{H}$ in (7.5) to solve for G, and plug the resulting expression into (7.4):

$$-R_2 \partial_x^5 Y - \left(2\pi \mathrm{i} + \frac{2\pi}{\Omega} \partial_x \right) \left[2\mathscr{H}^{-1} \left(2\pi \mathrm{i} Y(x) + \frac{2\pi}{\Omega} \partial_x Y(x) \right.\right.$$
$$\left.\left. - E(x) J\left(2\pi \mathrm{i} Y(x) + \frac{2\pi}{\Omega} \partial_x Y(x) \right) \right) \right] = 0. \tag{7.7}$$

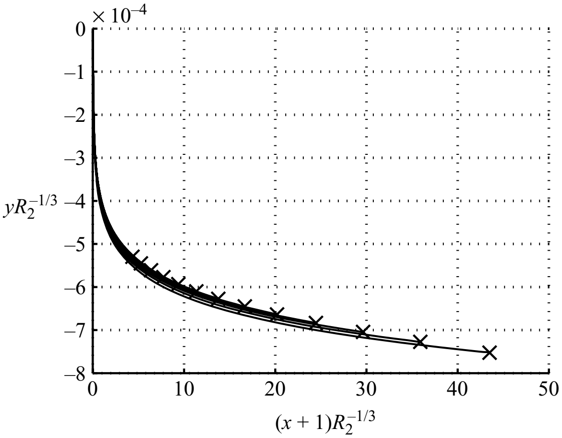

FIGURE 7. Fin shapes for $\Omega = 0.063$ and twenty values of R_2 ranging from 10^{-4} to 10^{-1}. The axes give the horizontal and vertical distances from the leading edge, divided by $R_2^{-1/3}$. The solutions collapse onto a similarity solution.

The boundary conditions are

$$Y|_{x=-1} = 0,\ \partial_x Y|_{x=-1} = \theta_0, \tag{7.8}$$

$$\partial_{xx} Y|_{x=1} = \partial_{xxx} Y|_{x=1} = 0, \tag{7.9}$$

$$R_2 \partial_{xxxx} Y|_{x=1} = -P|_{x=1} = 0. \tag{7.10}$$

Although complicated, (7.7) is linear in Y.

7.1. *Small flapping frequency*

We consider first the limit of small Ω, the steady case of (7.7), which consists of a fin held oblique to and bent over in a steady flow. Here (7.7) becomes

$$-R_2\partial_x^5 R - \left(\frac{2\pi}{\Omega}\partial_x\right)\left[2\mathscr{H}^{-1}\left(\frac{2\pi}{\Omega}\partial_x R(x) - E(x)J\left(\frac{2\pi}{\Omega}\partial_x R(x)\right)\right)\right] = 0. \tag{7.11}$$

This recalls a similar problem in which a fibre is held at its midpoint at a 90° angle to a steady inviscid flow. Solutions for small R_2 collapsed onto a similarity solution at the midpoint with length scale $\sim R_2^{1/3}$ (Alben, Shelley & Zhang 2002, 2004). The present problem differs in that the body is nearly aligned with the flow at the leading edge, and that therefore the wake can be modelled as a one-dimensional vortex sheet instead of a two-dimensional wake behind a bluff body in the earlier problem. Here we again find a similarity solution with a shrinking length scale $\sim R_2^{1/3}$ near the leading edge. For $R_2 \ll 1$, a dominant balance between the first two terms (with highest x-derivatives) on the left-hand side of equation (7.11) predicts the length scale X:

$$R_2 \frac{R}{X^5} \sim \frac{R}{X^2\Omega^2} \Rightarrow X \sim R_2^{1/3}\Omega^{-2/3}. \tag{7.12}$$

In figure 7, we plot the fin shape for $\Omega = 0.063$, with lengths divided by $R_2^{1/3}$. The plot shows that as we vary R_2, and consider the fin deflection at a fixed value of $(x+1)R_2^{-1/3}$, the fin deflection scales as $R_2^{-1/3}$. As R_2 increases to $O(1)$, the similarity solution transitions to a straight fin oblique to the flow.

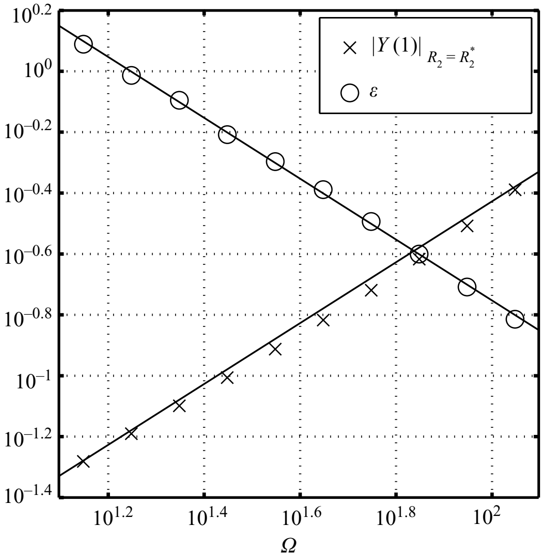

FIGURE 8. The maximum values and half-widths of the largest resonant peak at $R_2 = R_2^*$ is plotted for Ω ranging between 14 and 140. The maxima are the values of the fin deflection at the trailing edge, $|Y(1)|$. The half-widths ϵ are the distance between R_2^* and the value of R_2 where $|Y(1)|$ equals 0.995 times its value at R_2^*. The maxima scale as Ω and the half-widths scale as $1/\Omega$.

7.2. *Large flapping frequency*

We consider here the case where Ω is large, corresponding to figures 2(*a*) and 4. In figure 8 we plot the values of $|Y(1)|$ at the first resonant peak ($R_2 \approx 60$) versus Ω. As Ω becomes large, we find that the peak values diverge as Ω, and the half-widths shrink to zero as $1/\Omega$.

In analogy with damped resonant systems, such as the linear beam or string in air with internal damping (Hauser 1965), the peaks seem to correspond to damped resonances, with damping $\sim 1/\Omega$. Put differently, the response is proportional to the reduced pitching frequency.

We obtain a guess for the form of the resonant fin shapes by observing from figure 4 that wavelengths become shorter as R_2 tends to 0. In figure 9 we plot the shapes corresponding to the first eleven peaks, and find that as k increases, they are well-approximated by sinusoidal functions on the interval $[0, \pi]$, with wavenumber increasing by one with each peak.

To understand the distribution of resonant values of R_2, it is convenient to make the boundary conditions homogeneous (Hauser 1965). This can be done by subtracting from $Y(x)$ in (7.7) the steady solution $R(x)$ that was found in §7.1, which satisfies the same boundary conditions as Y. Subtracting (7.11) from (7.7), we find that the difference $Z(x) = Y(x) - R(x)$ satisfies

$$-R_2 \partial_x^5 Z - \left(2\pi\mathrm{i} + \frac{2\pi}{\Omega}\partial_x\right)\left[2\mathscr{H}^{-1}\left(2\pi\mathrm{i}Z(x) + \frac{2\pi}{\Omega}\partial_x Z(x)\right.\right.$$
$$\left.\left.- E(x)J\left(2\pi\mathrm{i}Z(x) + \frac{2\pi}{\Omega}\partial_x Z(x)\right)\right)\right] = S(x). \quad (7.13)$$

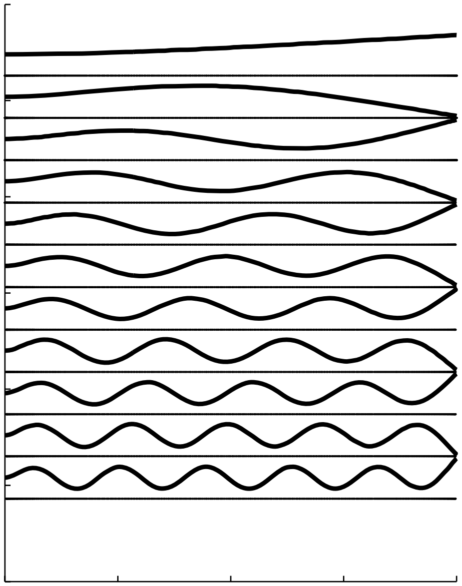

FIGURE 9. The fin shapes corresponding to the first 11 resonances in R_2, decreasing from $R_2 = 60$ to $R_2 = 6.5 \times 10^{-5}$. Here $\Omega = 420$. The shape amplitudes are scaled to have uniform absolute value at the trailing edge, which removes the overall growth $|Y(1)| \sim R_2^{0.4}$. The shorter-wavelength shapes are well-approximated on the interior of the interval by sinusoidal functions, which increase by one in wavenumber with each resonance. Only the (dominant) imaginary part of Y in (7.7) is plotted. The real part shows similar behaviour.

Equation (7.13) is the same as (7.7) but with the inhomogeneous term $S(x)$, and homogeneous boundary conditions. $S(x)$ consists of the remainder terms when subtracting (7.11) from (7.7):

$$S(x) = -(2\pi\mathrm{i})\left[2\mathscr{H}^{-1}\left(2\pi\mathrm{i}(-R(x)) + \frac{2\pi}{\Omega}\partial_x(-R(x)) - E(x)J\left(2\pi\mathrm{i}(-R(x)) + \frac{2\pi}{\Omega}\partial_x(-R(x))\right)\right)\right] - \frac{2\pi}{\Omega}\partial_x\left[2\mathscr{H}^{-1}\left(2\pi\mathrm{i}(-R(x)) - E(x)J\left(2\pi\mathrm{i}(-R(x))\right)\right)\right]. \quad (7.14)$$

In the limit of large Ω, (7.13) simplifies to:

$$-R_2\mathscr{H}\left(\partial_x^5 Z\right) + 8\pi^2 Z(x) - E(x)J\left(2\pi\mathrm{i}Z(x)\right) = S(x), \quad (7.15)$$

with boundary conditions

$$Z|_{x=-1} = \partial_x Z|_{x=-1} = 0; \qquad \partial_{xx} Z|_{x=1} = \partial_{xxx} Z|_{x=1} = \partial_{xxxx} Z|_{x=1} = 0. \quad (7.16)$$

The right-hand side $S(x)$ is a fixed function depending on R_2 and Ω but not Z. A resonance is obtained for values of R_2 such that the homogeneous part of (7.15) (the equation with right-hand side equal to zero) has a solution. In the limit that R_2 approaches such a resonant value, the left-hand side would approach zero, except that it must equal the fixed right-hand side. This is only possible if the amplitude of Z diverges.

We can now determine the asymptotic distribution of the resonant values of R_2 when R_2 is small by searching for an approximate solution to the homogeneous part of (7.15). We expand Z as a Chebyshev series,

$$Z(x) = \sum_{j=1}^{n} z_j \cos(j\phi); \quad x = \cos(\phi). \tag{7.17}$$

We can express the fifth x-derivative in (7.15) in terms of ϕ-derivatives:

$$\partial_x^5 = \left[-\frac{105c^4}{s^9} - \frac{90c^2}{s^7} - \frac{9}{s^5}\right]\partial_\phi + \left[\frac{105c^3}{s^8} + \frac{55c}{s^6}\right]\partial_\phi^2 + \left[-\frac{45c^2}{s^7} - \frac{10}{s^5}\right]\partial_\phi^3 + \frac{10c}{s^6}\partial_\phi^4 - \frac{1}{s^5}\partial_\phi^5; \quad c = \cos\phi, s = \sin\phi. \tag{7.18}$$

We insert the expansion (7.17) into each of the three terms on the left-hand side of (7.15). For the first term, we apply the differential operator (7.18). We expand $\partial_x^5 Z$ in a sin series, and obtain integer powers of j up to five multiplying $\sin j\theta$, for each j. Multiplication by the sin and cos prefactors in (7.18) cause the jth coefficient in the sin series for $\partial_x^5 Z$ to be a linear combination of $z_{j-13}, z_{j-12}, \ldots, z_{j-13}$, but the highest power is still a fifth power. Taking the Hilbert transform of $\partial_x^5 Z$ in (7.15) changes the sin series to a cos series. For the second term on the left-hand side of (7.15), we simply multiply the cos series for Z (7.17) by $8\pi^2$. The third term on the left-hand side of (7.15) is a weighted integral of Z (7.3), which integrates to zero against all modes z_j for j higher than 2.

In terms of the modes z_j, j higher than 2, we can disregard the third term, and (7.15) becomes

$$-R_2 \sum_{k=-13}^{13} z_{j+k} P_k^5(j) + 8\pi^2 z_j = 0, \qquad j = 3 \ldots n \tag{7.19}$$

where $P_k^5(j)$ is polynomial of up to fifth degree in j. The resonances are the values of R_2 corresponding to non-zero solutions $\{z_j\}$. For large j we therefore expect a resonance when $R_2 j^5 \sim$ const. In figure 10 we plot the values of R_2 for the first 100 resonances. At larger values of j we find the expected scaling $R_2 \sim j^{-5}$.

To determine the peak *values* of fin deflection $|Y(1)|$, circulation $|\Gamma_0|$, and input and output power shown in figure 10, we must consider their dependence on Ω. We therefore turn now to the damping terms in (7.13) in the limit of large Ω, retaining the lowest order terms in $1/\Omega$:

$$-R_2\partial_x^5 Z + 8\pi^2\mathscr{H}^{-1}(Z(x)) + \frac{4\pi \mathrm{i}}{\Omega}\left(\partial_x\mathscr{H}^{-1}(Z(x)) + \mathscr{H}^{-1}\partial_x Z(x)\right) = E(x)J\left(2\pi \mathrm{i} Z(x) + \frac{2\pi}{\Omega}\partial_x Z(x)\right) + S(x). \tag{7.20}$$

We first explain the Ω scaling of the resonant peaks and the $1/\Omega$ scaling of their half-widths, shown in figure 8. At a resonant value of $R_2 = R_2^*$, the first two terms on the left vanish. The balance between the third term and the right-hand side implies $Z(x) \sim \Omega$, so the amplitudes of the resonant peaks grow linearly with Ω. The half-widths of the resonant peaks can be estimated by inserting $R_2 = R_2^* + \epsilon$ into (7.20), and finding what perturbation ϵ makes the sum of the first two terms comparable to the third (damping) term. At R_2^*, the first two terms cancel, which leaves $-\epsilon\partial_x^5 Z \approx (4\pi \mathrm{i}/\Omega)\left(\partial_x\mathscr{H}^{-1}(Z(x)) + \mathscr{H}^{-1}\partial_x Z(x)\right)$. Thus the half-widths of the resonant peaks are $\epsilon \sim C/\Omega$.

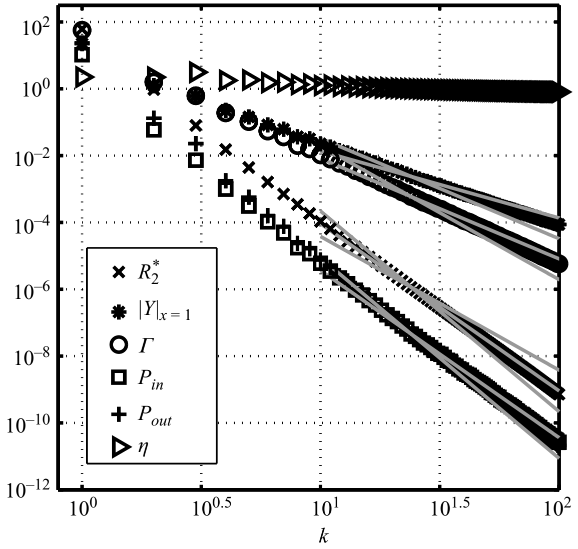

FIGURE 10. For the first 100 resonant peaks in R_2 at $\Omega = 420$, the values of dimensionless rigidity R_2^*, trailing-edge deflection $|Y(1)|$, circulation $|\Gamma_0|$, input power $\langle P_{in}\rangle$, output power $\langle P_{out}\rangle$, and efficiency η. The values are plotted versus the index of the resonance. The values of rigidity R_2^* (crosses) are plotted with the lines corresponding to power laws $\sim k^{-4}, k^{-5}, k^{-6}$. A good fit is obtained for large k by the k^{-5} line. The trailing-edge deflection $|Y|_{x=1}$ (asterisks) is plotted with fit lines $\sim k^{-2}, k^{-3}$ and falls between these lines. The circulation Γ (circles) is plotted with fit lines $\sim k^{-3}, k^{-4}$ and falls between these lines. The input and output power (squares and plusses, respectively) are plotted with fit lines $\sim k^{-5}, k^{-6}$ and both are best fit by the k^{-5} line for large k. The efficiency, which is the ratio of the two, thus approaches a constant value for large k.

Having explained the distribution of resonances with respect to R_2, and seen that the fin shape Y at each resonance corresponds to an approximately sinusoidal function with wavenumber k increasing by one, we now discuss the scaling of quantities in figure 10 with k. At a resonance, the first two terms of (7.20) cancel. For $Z \sim \sin kx$, the third term in (7.20) scales as kZ, while the dominant term on the right-hand side is an integral of Z (the operator J), which scales as C/k for a constant C. This balance of terms predicts $Z \sim Ck^{-2}$. We note that R is sub-dominant to Z at a resonance, since R remains bounded. Considering $Y = Z + R$, we thus expect Y to show the same dependence on k as Z. Figure 10 shows that $|Y(1)| \sim k^{\alpha}$ where $-2 > \alpha > -3$, which is a somewhat faster decay than predicted by this argument. In this argument we have neglected the function $E(x)$ multiplying J, which affects the balance of the sinusoidal modes and the function $S(x)$.

Given the scaling of Y, we expect that $|\Gamma_0|$ should scale as Y/k, from its expression as an integral of Y in (7.2). Figure 10 shows this to be approximately correct. Figure 10 also shows that the input and output power scale as k^{-5}. This can be explained by expressing both quantities as products of R_2 with functions of the shape of the fin at the driving end. The input power in (5.17) already has this form. The output power in (5.18) can be put in this form by first noting that the second term on the left-hand side of (5.18) is dominant over the first term (the leading-edge suction). By inserting $R_2\partial_x^4 Y$ for P in the second term (using (4.2)), and integrating the term by parts, we obtain

$$\int_{-1}^{1} -R_2 \partial_x^4 Y \partial_x Y \, \mathrm{d}x = \left[-R_2 \partial_x^3 Y \partial_x Y\right]_{-1}^{1} + \int_{-1}^{1} R_2 \partial_x^3 Y \partial_x^2 Y \, \mathrm{d}x \tag{7.21}$$

$$= R_2 \left(\frac{1}{2} \left(\partial_x^2 Y\right)^2 + \theta_0 \partial_x^3 Y \right) \bigg|_{x=-1} \tag{7.22}$$

where we have applied the boundary conditions (4.4) to obtain the second equation. We have already found that $R_2 \sim k^{-5}$. It turns out that the shape terms at the leading edge are nearly constant with respect to R_2. Thus P_{in} and P_{out} inherit the k^{-5} scaling of R_2. Consequently the efficiency is $O(1)$ for large k. In (6.1), the scalings of the peaks of P_{in} and P_{out} are somewhat slower than linear in R_2. However, these exponents are based on just the first several peaks. Figure 10 shows values at the first 100 peaks and gives a more accurate estimate of the asymptotic scalings: $P_{in} \sim R_2$ and $P_{out} \sim R_2$ at small R_2.

Combining the trailing-edge scaling $|Y(1)| \sim k^{-5/2}$ with those for input and output power, we find that P_{in} and $P_{out} \sim |Y(1)|^2$, which is to be expected in the linearized theory, where power is a quadratic function of body shape.

8. Comparison

In § 6, figure 3 we have plotted the optimal values of R_2 versus Ω for maximum thrust power and maximum efficiency. Here we give data for some typical fish fins and insect wings. Relatively few studies have measured the rigidity of these structures. We focus on two organisms for which the values of R_2 and Ω can be computed from studies which have measured the rigidity and kinematics of thrust-bearing appendages.

Combes & Daniel (2003*b*) measured the chordwise bending rigidity in wings of the hawkmoth Manduca Sexta. Flexural rigidity is highly non-uniform, decreasing by about an order of magnitude from the leading edge to the trailing edge. We take the value of flexural rigidity measured at the leading edge, $B = 10^{-5}$–2×10^{-6} N m^2 in 10 measurements of male forewings. The area density ρ_f of the fluid is 1.2 kg m^{-3} (air in normal atmospheric conditions) times the span of the wing, 0.04 m. The chord length of the wing is $L = 2 \times 10^{-2}$ m. The typical flapping frequency is $\omega = 2\pi \times 26$ Hz. Willmott & Ellington (1997) gave the same ω, and found that it varies by less than 10 % over a range of typical flight speeds $U = 0.4 - 5.7\,\mathrm{m\,s^{-1}}$. Combining these parameters in the definitions of R_2 and Ω above (2.6), we find $R_2 = 0.49 - 2.5$ (with the range inherited from B), and $\Omega = 0.57 - 8.16$ (with the range inherited from U).

We have delineated this range of (Ω, R_2) space as the solid box in figure 3. We find that the rigidities are about two orders of magnitude below the optimal values for thrust power, and intersect the values for optimal efficiency. The data of Combes & Daniel (2003*b*) also show that spanwise rigidity is one to two orders of magnitude higher than chordwise rigidity, and hence closer to our optimal thrust line. Spanwise bending may be more important for take-offs, particulary in 'clap and fling' mechanisms (Ellington 1984), than in steady flight.

The bluegill sunfish has been the subject of numerous studies of swimming kinematics by Lauder and others (Shadwick & Lauder 2006). Recently the bending rigidity of fin rays in the pectoral fin have been measured (Alben *et al.* 2007) as $B = 10^{-5}\,\mathrm{N\,m^2}$. The area density ρ_f of the fluid is 917 kg m^{-3} (fresh water at room temperature) times the span of the fin, 0.04 m. Typical swimming speeds are $U = 0.054 - 0.18\,\mathrm{m\,s^{-1}}$, which scales roughly in proportion to the fin beat frequencies $\omega = 2\pi \times 1 - 2$ Hz (Gibb, Jayne & Lauder 1994). Combining these parameters, we find

$R_2 = 0.017 - 0.067$ (with the range inherited from ω) and $\Omega = 1.4 - 9.3$. This range of (Ω, R_2) is shown by the dashed box in figure 3. We find again that the values of R_2 are well below those for optimal thrust. We note that in the bluegill sunfish the pectoral fin is used for high-efficiency, low-speed swimming, while the tail fin is used for fast-burst swimming.

For both the hawkmoth and bluegill sunfish, the kinematics involve considerable heaving as well as pitching, but as stated previously, we expect the optimal flexibility for pitching to be similar to that for heaving-plus-pitching in the model. Furthermore, three-dimensional geometry, kinematics and flow effects are important for both organisms, as well as effects due to large-amplitude motions, such as leading-edge separation. We therefore do not expect agreement with our model closer than the level of order of magnitude. However, we find that an order-of-magnitude comparison gives a useful context for our results.

9. Conclusions

We have presented a new formulation of the motion of a flexible body in the presence of vortex sheets, building on the work of Jones (2003) and Alben & Shelley (2008). We have used this formulation to study propulsive forces generated by a flexible body pitched periodically at the leading edge in the small amplitude regime. We find that the thrust power generated by the body has a series of resonant peaks with respect to R_2, the highest of which is the optimum for thrust power and corresponds to a body flexed upwards at the trailing edge in an approximately one-quarter-wavelength mode of deflection. Subsequent peaks correspond to higher-wavenumber modes of the fin, which are approximately sinusoidal. The size of the peaks is proportional to reduced pitching frequency Ω, and their half-widths scale as $1/\Omega$. The optimal efficiency approaches 1 as R_2 becomes small. As R_2 becomes large, the efficiency decreases to 30–50 % depending on Ω. The optimal flexibility for thrust power increases from $R_2 \approx 60$ for large Ω to $R_2 = \infty$ (a rigid body) for $\Omega = 0.27$. For $\Omega < 0.22$, only negative thrust power, i.e. drag, is possible.

We have been able to derive the power-law scalings by analysing the fin as a resonant system. In the limit of small Ω, we have steady solutions which are self-similar at the leading edge in the limit of small R_2. They collapse onto a single shape which is somewhat like a reed bent in a steady wind. In the limit of large Ω, we find that the distribution of resonant rigidities is $R_2 \sim k^{-5}$, corresponding to fin shapes with wavenumber k. Corresponding power laws are $P_{in} \sim k^{-5} \sim R_2$, $P_{out} \sim k^{-5} \sim R_2$, trailing-edge deflection $|Y(1)| \sim k^{-2} \sim R_2^{0.4}$, and shed circulation strength $|\Gamma_0| \sim k^{-3} \sim R_2^{0.6}$. The height and half-widths of each resonant peak are shown to scale as Ω and $1/\Omega$, respectively.

For comparison, we have computed the range of R_2 and Ω from available data on the hawkmoth forewing and the bluegill sunfish pectoral fin. We find that the rigidities are closer to the maximum efficiency values than to the maximum thrust values of the model. The kinematics and geometry of these systems differ from the two-dimensionality we have assumed.

Appendix. Comparison of full model and linearized periodic model

Here we give a verification that we have correctly derived the linearized, periodic version of the fully nonlinear problem in §2. In figure 11 we compare the results of fully nonlinear simulations of the initial value problem with the periodic problem described in §4. We plot the trailing-edge deflection $y_{\max}$ and the circulation $\Gamma_{\max}$

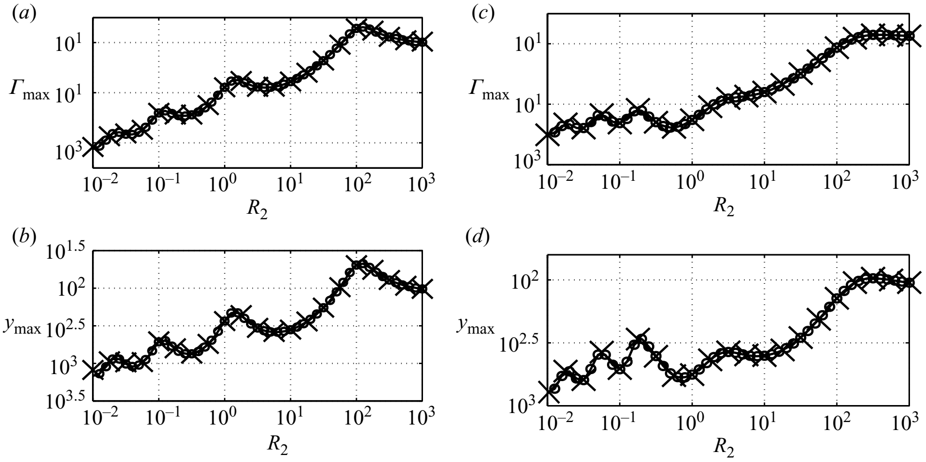

FIGURE 11. Comparison between the full and linearized models, with $\theta_0 = \pi/720$. The values compared are the maximum vertical deflection at the trailing edge $y_{\max}$, and the maximum of the circulation $\Gamma_{\max}$, over periods 5 to 10 after startup for the full model, and over the period of the periodic model. Values for the full model are plotted with crosses and values for the linearized model are plotted with circles. Panels (*a*) and (*b*) correspond to $\Omega = 4.2$, and panels (*c*) and (*d*) correspond to $\Omega = 1.4$.

for two values of Ω over many decades of R_2. This comparison provides a check that we have correctly linearized the problem, and that in particular the semi-infinite vortex sheet wake assumed in § 2 is a good approximation to a finite sheet in the fully nonlinear initial value problem. We shall give further details of the fully nonlinear problem in a subsequent work.

REFERENCES

ALBEN, S., MADDEN, P. G. & LAUDER, G. V. 2007 The mechanics of active fin-shape control in ray-finned fishes. *J. R. Soc. Interface* **4** (13), 243–256.

ALBEN, S. & SHELLEY, M. J. 2005 Coherent locomotion as an attracting state for a free flapping body. *Proc. Natl Acad. Sci. USA* **102** (32), 11163–11166.

ALBEN, S., SHELLEY, M. & ZHANG, J. 2002 Drag reduction through self-similar bending of a flexible body. *Nature* **420**, 479–481.

ALBEN, S., SHELLEY, M. & ZHANG, J. 2004 How flexibility induces streamlining in a two-dimensional flow. *Phys. Fluids* **16**, 1694.

ALBEN, S. & SHELLEY, M. J. 2008 Flapping states of a flag in an inviscid fluid: bistability and the transition to chaos. *Phys. Rev. Lett.* **100**, 74301.

ANTMAN, S. S. 1995 *Nonlinear Problems of Elasticity*. Springer.

BAINBRIDGE, R. 1963 Caudal fin and body movement in the propulsion of some fish. *J. Exp. Biol.* **40** (1), 23–56.

BERGOU, A. J., XU, S. & WANG, Z. J. 2007 Passive wing pitch reversal in insect flight. *J. Fluid Mech.* **591**, 321.

CHILDRESS, S. 1981 *Mechanics of Swimming and Flying*. Cambridge University Press.

CHILDRESS, S., VANDENBERGHE, N. & ZHANG, J. 2006 Hovering of a passive body in an oscillating airflow. *Phys. Fluids* **18**, 117103.

COMBES, S. A. & DANIEL, T. L. 2003*a* Flexural stiffness in insect wings I. Scaling and the influence of wing venation. *J. Exp. Biol.* **206** (17), 2979–2987.

COMBES, S. A. & DANIEL, T. L. 2003*b* Flexural stiffness in insect wings II. Spatial distribution and dynamic wing bending. *J. Exp. Biol.* **206** (17), 2989–2997.

Didden, N. 1979 On the formation of vortex rings: Rolling-up and production of circulation. *Z. Angew. Mathe. Phys.* **30** (1), 101–116.

Ellington, C. P. 1984 The aerodynamics of hovering insect flight. III. Kinematics. *Phil. Trans. R. Soc. Lond. B* **305**, 41–78.

Fish, F. E. & Lauder, G. V. 2006 Passive and active flow control by swimming fishes and mammals. *Annu. Rev. Fluid Mech* **38**, 193–224.

Fish, F. E., Nusbaum, M. K., Beneski, J. T. & Ketten, D. R. 2006 Passive cambering and flexible propulsors: cetacean flukes. *Bioinspiration and Biomimetics,* **1** (4), S42–S48.

Gibb, A., Jayne, B. & Lauder, G. 1994 Kinematics of pectoral fin locomotion in the bluegill sunfish Lepomis Macrochirus. *J. Exp. Biol.* **189** (1), 133–61.

Godoy-Diana, R., Aider, J. L. & Wesfreid, J. E. 2008 Transitions in the wake of a flapping foil. *Phys. Rev.* E **71**, 016308.

Hauser, W. 1965 *Introduction to the Principles of Mechanics*. Addison-Wesley.

Jones, M. 2003 The separated flow of an inviscid fluid around a moving flat plate. *J. Fluid Mech.* **496**, 405–401.

Katz, J. & Weihs, D. 1978 Hydrodynamic propulsion by large amplitude oscillation of an airfoil with chordwise flexibility. *J. Fluid Mech.* **88** (3), 485–497.

Katz, J. & Weihs, D. 1979 Large amplitude unsteady motion of a flexible slender propulsor. *J. Fluid Mech.* **90** (4), 713–723.

Lauder, G. V., Madden, P. G. A., Mittal, R., Dong, H. & Bozkurttas, M. 2006 Locomotion with flexible propulsors: I. Experimental analysis of pectoral fin swimming in sunfish. *Bioinspiration and Biomimetics,* **1** (4), S25–S34.

Lian, Y., Shyy, W., Viieru, D. & Zhang, B. 2003 Membrane wing aerodynamics for micro air vehicles. *Prog. Aero. Sci.* **39** (6-7), 425–465.

Lighthill, J. M. 1969 Hydromechanics of aquatic animal propulsion. *Annu. Rev. Fluid Mech.* **1**, 413–446.

Lighthill, M. J. 1960 Note on the swimming of slender fish. *J. Fluid Mech.* **9** (2), 305–317.

Liu, P. & Bose, N. 1997 Propulsive performance from oscillating propulsors with spanwise flexibility. *Proc. R. Soc. Lond.* A **453**, 1763–1770.

Long, J., Hale, M., Mchenry, M. & Westneat, M. 1996 Functions of fish skin: flexural stiffness and steady swimming of longnose gar, Lepisosteus osseus. *J. Exp. Biol.* **199** (Pt 10), 2139–51.

Mason, J. C. & Handscomb, D. C. 2003 *Chebyshev polynomials*. Chapman/Hall/CRC.

Miao, J. M. & Ho, M. H. 2006 Effect of flexure on aerodynamic propulsive efficiency of flapping flexible airfoil. *J. Fluid. Struct.* **22** (3), 401–419.

Muskhelishvili, N. I. 1953 *Singular Integral Equations: Boundary Problems of Function Theory and their Application to Mathematical Physics*. P. Noordhoff.

Nitsche, M. & Krasny, R. 1994 A numerical study of vortex ring formation at the edge of a circular tube. *J. Fluid Mech.* **276**, 139–161.

Prempraneerach, P., Hover, F. S. & Triantafyllou, M. S. 2003 The effect of chordwise flexibility on the thrust and efficiency of a flapping foil. In *International Symposium on Unmanned Untethered Submersible Technology*.

Pullin, D. I. & Perry, A. E. 1980 Some flow visualization experiments on the starting vortex. *J. Fluid Mech.* **97**, 239–255.

Pullin, D. I. & Wang, Z. J. 2004 Unsteady forces on an accelerating plate and application to hovering insect flight. *J. Fluid Mech.* **509**, 1–21.

Ralston, A. & Rabinowitz, P. 2001 *A First Course in Numerical Analysis*. Dover.

Saffman, P. 1992 *Vortex Dynamics*. Cambridge University Press.

Shadwick, R. E. & Lauder, G. V. 2006 *Fish Biomechanics*. Academic.

Sparenberg, J. A. 2002 Survey of the mathematical theory of fish locomotion. *J. Eng. Math.* **44** (4), 395–448.

Thwaites, B. 1987 *Incompressible Aerodynamics: An Account of the Theory and Observation of the Steady Flow of Incompressible Fluid past Aerofoils, Wings, and Other Bodies*. Dover.

Triantafyllou, M. S., Triantafyllou, G. S. & Gopalkrishnan, R. 1991 Wake mechanics for thrust generation in oscillating foils. *Phys. Fluids* A **3** (12), 2835–2837.

Triantafyllou, M. S., Triantafyllou, G. S. & Yue, D. K. P. 2000 Hydrodynamics of fishlike swimming. *Ann. Rev. Fluid Mech.* **32**, 33–53.

Vandenberghe, N., Zhang, J. & Childress, S. 2004 Symmetry breaking leads to forward flapping flight. *J. Fluid Mech.* **506**, 147–155.

Videler, J. J. 1993 *Fish Swimming*. Springer.

Wainwright, S. A. 2000 The animal axis. *Am. Zool.* **40** (1), 19–27.

Willmott, A. P. & Ellington, C. P. 1997 The mechanics of flight in the hawkmoth Manduca sexta. I. Kinematics of hovering and forward flight. *J. Exp. Biol.* **200** (21), 2705–22.

Wu, T. Y. 1961 Swimming of a waving plate. *J. Fluid Mech.* **10** (3), 321–344.